nature materials

SUPPLEMENTARY INFORMATION

DOI: 10.1038/NMAT2595

A Silicon-Based Electrical Source of Surface Plasmon Polaritons

R. J. Walters[1], R. V. A. van Loon[1], I. Brunets[2], J. Schmitz[2], A. Polman[1]

[1]Center for Nanophotonics, FOM Institute for Atomic and Molecular Physics, Science Park 113, 1098 XG Amsterdam, The Netherlands

[2]MESA+ Institute for Nanotechnology, University of Twente, P.O. Box 217, 7500 AE Enschede, The Netherlands

1. Coupling between silicon nanocrystals and the Au/(100 nm Al_2O_3)/Au MIM waveguide

Here we present additional details of a model for the coupling between silicon nanocrystals and the modes of the Au/(100 nm Al_2O_3)/Au MIM waveguide structure in our experiments, using the classical model developed by Ford and Weber [1].

Table S1. Measured dielectric properties for gold.

Wavelength (nm)	$Re\{\varepsilon\}$	$Im\{\varepsilon\}$
600.00	-9.72	1.27
650.00	-13.31	1.07
700.00	-17.13	1.05
750.00	-21.08	1.19
800.00	-25.18	1.48
850.00	-29.60	1.76
900.00	-34.04	1.88
950.00	-38.94	2.38

Silicon nanocrystals in our device are embedded in alumina ($\varepsilon = 2.9$) at distances of 20, 40, 60, and 80 nm from the bottom Al_2O_3/Au interface. Table S1 shows the optical properties of gold used in our calculations. These values were measured using variable-angle spectral ellipsometry for gold layers grown on monitor wafers during fabrication.

Using the symmetry of the waveguide, we model the four nanocrystal layers in the device by studying the power radiated by dipoles located at 20 nm and 40 nm from the bottom Al_2O_3/Au interface. In Figure S1, we show the differential power radiated by dipoles at these positions for an emission frequency corresponding to a free space wavelength (λ_0) of 800 nm. The differential power is normalized to the total power that would be radiated by the dipole in a uniform alumina medium (according to the Larmor equation [2]) and plotted against the in-plane wave vector component $k_{||}$, normalized to the free space wave vector k_0. A single peak is observed in the differential radiated power spectrum at $k_{||}/k_0 = 2.15$, which is the effective index of the symmetric-H_y plasmon mode for this waveguide geometry. In Figure S2, we have repeated similar calculations of the differential radiated power for dipoles centered in a series of waveguides with varying alumina layer thickness.

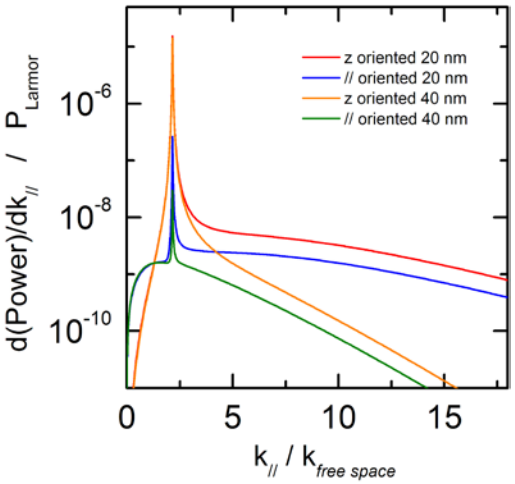

Figure S1. Power dissipated by oriented dipoles inside a Au/(100 nm Al_2O_3)/Au MIM waveguide. The differential power radiation spectrum of dipoles emitting at $\lambda_0 = 800$ nm inside the experimental MIM waveguide geometry is shown versus the in-plane wave vector component of the emitted radiation. The peak at $k_{||}/k_0 = 2.15$ corresponds to the symmetric-H_y MIM plasmon mode.

In these calculations we model the power dissipated by randomly oriented dipoles by taking the weighted average of the result for a perpendicularly-oriented dipole and the result for a dipole oriented parallel to the waveguide. The mode structure of the waveguide series is separately

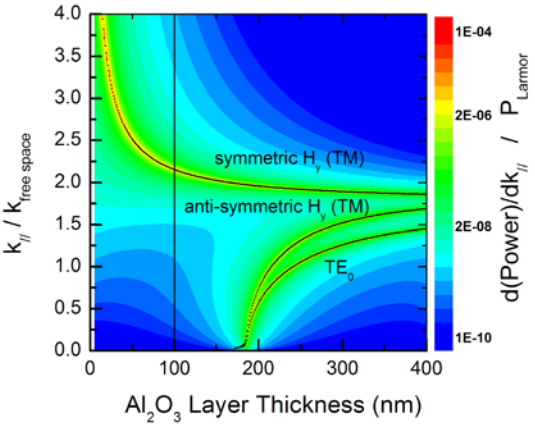

Figure S2. Dipole power dissipation in a series of Au/Al_2O_3/Au waveguides. The differential power radiated by randomly oriented dipoles centered in a series of waveguides is shown versus the in-plane wave vector component and the thickness of the Al_2O_3 layer for emission at $\lambda_0 = 800$ nm. The effective indices of the corresponding waveguide modes are overlaid. The line at 100 nm represents our (single mode) device geometry.

DOI: 10.1038/NMAT2595

calculated as described in [3] and [4] and drawn over the differential power radiation intensity map. It is apparent that the peaks in the differential power spectrum correspond to the mode structure of the waveguide. The peak in Figure S1 can be assigned to the symmetric-H_y plasmon mode. Note that Au/Al_2O_3/Au MIM waveguides support only this single plasmonic mode when the layer thickness is less than ~150 nm (as in our experiment). We find that silicon nanocrystals couple efficiently to the symmetric-H_y waveguide mode when positioned inside the waveguide at distances greater than ~10 nm from the gold layer. Our calculations are in agreement with similar results reported recently by Hryciw *et al.* [5].

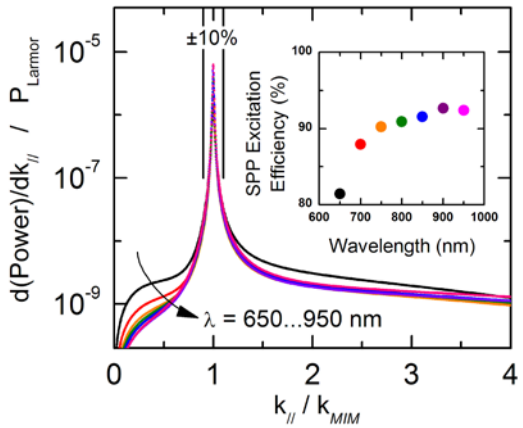

Figure S3. Coupling strength between silicon nanocrystals and MIM waveguide plasmons for λ_0 = 650 – 900 nm. The fraction of total dissipated power emitted at in-plane wave vectors near the SPP mode is a measure for the fraction of quantum dot emission that is coupled to SPPs. The coupling efficiency is only weakly dependent on wavelength (inset).

In Figure S3, we show the average power dissipation for a collection of dipoles representing the silicon nanocrystals in our device at the wavelengths of interest (650 — 950 nm). We assume the dipoles are randomly oriented and distributed evenly in the four grown layers at 20, 40, 60, and 80 nm from the bottom Au/Al_2O_3 interface. In this figure, we have normalized the in-plane wave vector to the value at the peak in the differential radiated power, k_{MIM}, corresponding to the symmetric-H_y plasmon mode of the MIM waveguide. We integrate the fraction of the total power emitted within ±10% of k_{MIM} as a measure of the silicon-nanocrystal-to-plasmon-mode coupling efficiency (Figure S3, inset). Power radiated at longer wave vectors is assigned to "lossy surface waves" which do not contribute to plasmon generation [6]. The coupling efficiency is only weakly dependent on wavelength; the calculated variation can not account for the oscillatory features shown in the manuscript in Figure 3 and Figure 4e-f. As discussed in the text, these features result from Fabry-Perot interference of SPPs within the passive section of the MIM waveguide.

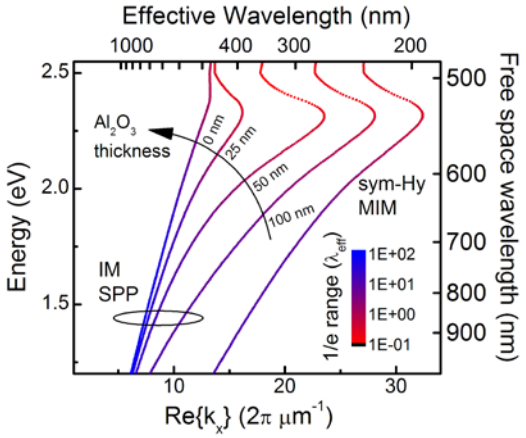

Figure S4. Dispersion diagrams for IM modes after cladding layer removal. When the top gold cladding layer is removed from the device, the remaining structure supports an IM plasmon mode with a longer effective wavelength than the MIM plasmon mode. This mode is sensitive to the thickness of the remaining Al_2O_3 layer. The color scale represents the 1/*e* propagation length normalized to the effective wavelength of the mode.

2. Feature design and FDTD simulations

We used finite difference time domain (FDTD) simulations to study two simple feature geometries. The first structure is a single slit cut through the bottom cladding layer of the waveguide. This feature is used to electrically isolate portions of the device while transmitting up to ~60% of the launched SPP power. The second feature is created by milling two parallel slits in the top cladding layer of the waveguide so as to define a thin metal bar. This structure scatters up to ~40% of the incident SPP power into the far field. The performance of these structures can be understood generally in terms of the SPP modes supported by the MIM waveguide and the Air/Al_2O_3/Au "IM" structure that remains when one of the gold cladding layers is removed.

Figure S4 shows that the effective wavelength of the IM SPP modes is dependent on the thickness of the (silicon nanocrystal doped) alumina layer that remains after FIB milling. The milling rate of gold varies with grain orientation, so some over-etching is necessary to ensure full removal of the metal from the slit area. A quantitative match between simulation and experiment would be difficult to establish because the uniformity of the partially removed alumina layer may be poor. Additionally, the effect of possible gallium implantation during FIB milling on the index of refraction of the alumina layer is unknown. A final difference between the simulated geometry and the fabricated geometry is the sidewall tapering caused by re-deposition during FIB milling. To clarify the operating principles of the isolation and out-coupling features, we will focus on simulations of idealized structures without tapering or over-

etching into the alumina. While the following discussion can be a useful guide for the design of similar electrical SPP sources, we note that the arguments we advance in our letter do not rely on these details. The isolation and out-coupling structures have been included in the FDTD calculations we show in Figure 3, in which we vary only the length of the Fabry-Perot cavity defined by the length of the passive MIM waveguide section.

3. Isolation Slits

The interaction of the symmetric-H_y MIM mode with the single slit isolation feature was modeled using two-dimensional full-field FDTD simulations for several slit widths, residual alumina layer thicknesses, and free space wavelengths using the commercial software package "Lumerical FDTD Solutions". We measured the transmitted and reflected power fraction using frequency domain power monitors placed 100 nm beyond the slit and 100 nm before the slit. Each wavelength was simulated independently by launching a ~10 fs long pulse in the calculated profile of the symmetric-H_y MIM mode (which varies slightly with wavelength) in a plane located 50 nm to the left of the slit. The scattered fraction of the inserted power was monitored by the total transmission across a parallel plane located 2 μm away from the surface of the waveguide. The grid cell size was 1 x 1 nm in the region of the slit, 2 x 1 nm inside the waveguide, and graded elsewhere. The total simulation area was 6 x 5 μm, with perfectly matched layers specified at the simulation boundaries. The total time duration of the simulation was set to 60 fs. This choice excludes effects that might be caused by small reflections from the simulation boundaries due to the finite group velocity of the pulse and the simulation size. A typical calculation using these parameters requires ~5 min of processing time when solving in parallel on a workstation with 2 quad-core Intel Nehalem-series processors and uses ~50 MB of working memory.

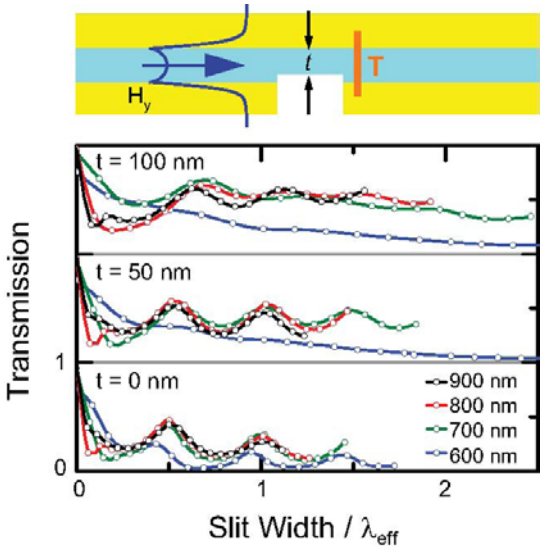

Figure S5. Transmission properties of isolation slits. The fraction of launched SPP power transmitted across an isolation slit is shown versus the length of the slit, normalized by the effective wavelength of the IM plasmon mode, for several free-space wavelengths and three residual Al_2O_3 layer thicknesses. We simulate the complete transmission spectrum for a slit with an Al_2O_3 layer thickness t = 100nm and a width of 300 nm in Figure S6.

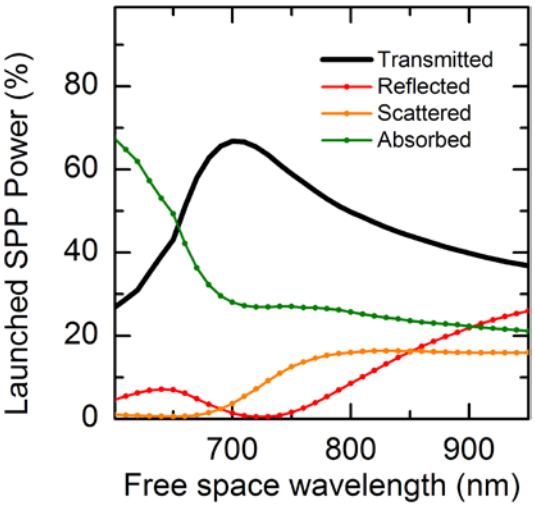

Figure S6. Spectral properties of an isolation slit. The transmitted, reflected, scattered, and absorbed fractions of the launched SPP power are simulated for an isolation slit of width 300 nm and residual Al_2O_3 layer thickness t = 100 nm. Note that no oscillations are observed in the transmission efficiency over the wavelength range emitted by the silicon nanocrystals in our experiment.

Figure S5 summarizes the simulation results by plotting the fraction of launched power that is transmitted against the dimensionless ratio of the isolation slit width to the effective wavelength of the IM mode in the slit region. Peaks in transmission are observed when the slit width (w) accommodates a round-trip resonance of the single-cladding layer IM plasmon mode ($2w = n\lambda_{eff}$). The oscillations are less visible at shorter wavelengths and in structures with thicker residual alumina layers after milling. These conditions correspond to slits that support IM modes that propagate with more loss (see Figure S4, inset color scale) and reflect less strongly from the interface with the MIM waveguide. Both of these effects decrease the visibility of the resonances. While the maximum transmission is observed for vanishingly narrow slits, this design strategy is not preferred because the slit must also perform an electrical isolation function. Instead, we select an isolation slit width near the first order resonance at the design wavelength.

The transmission spectrum of an isolation slit with a width of 300~nm is shown in Figure S6, with additional curves showing the reflected, scattered, and absorbed power fractions. The absorption is

DOI: 10.1038/NMAT2595

calculated by subtracting the power transmitted across the three monitor planes corresponding to reflection, transmission, and scattered power from the launched power. Note that the isolation feature does not exhibit oscillating spectral features in transmission over the wavelengths emitted by the silicon nanocrystals.

4. Out-coupling Features

We fabricated out-coupling features consisting of two symmetrically milled adjacent slits that define a thin metal bar. This structure can scatter more power out of the waveguide than a single milled slit and still has a well-defined location. An SEM image of an out-coupling feature in cross section is shown in Figure S7.

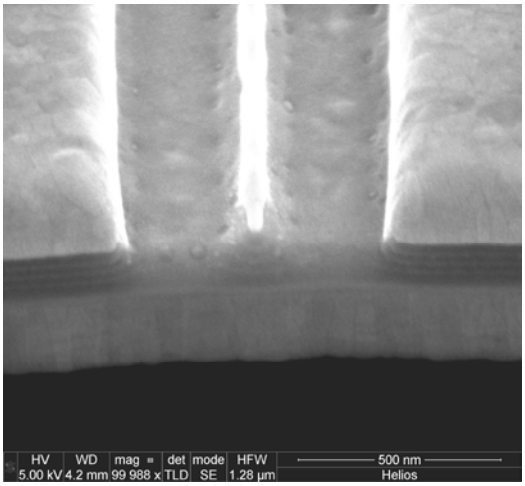

Figure S7. SEM cross-section of an out-coupling test feature fabricated by FIB milling.

We used 2D FDTD simulations to model the scattering performance of the out-coupling feature, following the same general approach described above for the transmission of isolation slits. Power is launched at each free space wavelength in the mode profile of the symmetric H_y plasmon mode and frequency domain power monitors are used to determine the transmission, reflection, and scattered power normalized to the source power. The absorption is modeled by the fraction of the launched power that is not detected by the three monitors.

In Figure S8, we show the simulated spectral variation in the out-coupling feature scattering efficiency for a structure with 150 nm wide slits and a 150 nm wide central bar. Note that no oscillations in the scattered power fraction are observed over the range of wavelengths emitted by the silicon nanocrystals.

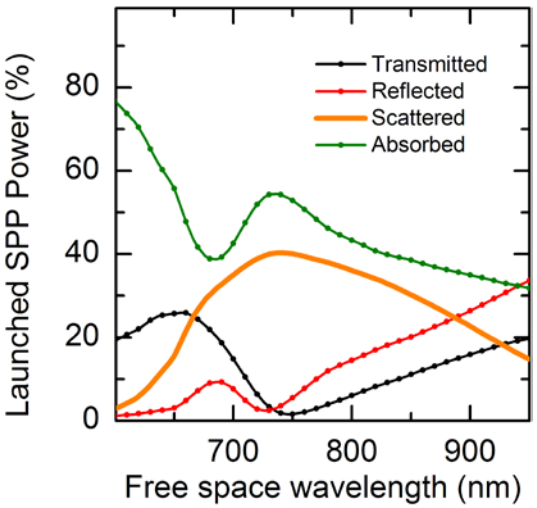

Figure S8. Spectral properties of an out-coupling feature. The transmitted, reflected, scattered, and absorbed fractions of the launched SPP power are simulated for an out-coupling feature with a central bar width of 150 nm surrounded by two slits of width 150 nm. The residual Al_2O_3 layer thickness is 100 nm. Note that no oscillations are observed in the scattering efficiency over the wavelength range emitted by the silicon nanocrystals in our experiment.

5. Peak data for all devices in Figure 4a-d

As discussed in the text, non-uniformity in the active Al_2O_3 layer of the device that contains the silicon nanocrystals results in deviations from the expected variation in intensity as the distance between the isolation slits and the out-coupling feature is varied. In Figure 4a-d, we draw the reader's attention to a region containing devices that do follow the expected trend, while acknowledging that other devices on this sample do not behave as expected. In Figure S10, we show the peak intensity data for all out-coupling devices seen in Figure 4a-d.

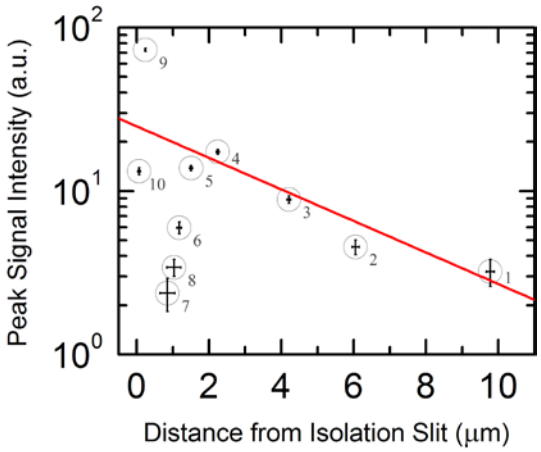

Figure S9. Peak intensity detected for all devices visible in Figure 4a-d. The red line is an exponential decay curve with the 1/*e* length fixed at the value expected for SPPs in our waveguide geometry (4.5 µm). The initial value is fit to the peak intensity values measured for devices 1—5. As discussed in the main text, non-uniformity in the source region of the device limits the conclusions we can draw from this analysis, as devices 6—10 clearly deviate from the model.

6. References

[1] *Electromagnetic interactions of molecules with metal surfaces.*
G.W. Ford and W. H. Weber, Phys. Rep. **113**, 195 (1984)

[2] Classical Electrodynamics (3rd edition).
J.D. Jackson. John Wiley & Sons: New York (1998). ISBN 0-471-30932-X.

[3] *Are negative index materials achievable with surface plasmon waveguides? A case study of three plasmonic geometries.*
J.A. Dionne, E. Verhagen, A.Polman, and H.A. Atwater, Optics Express **16**, 19001 (2008)

[4] *Plasmon slot waveguides: towards chip-scale propagation with subwavelength-scale localization.*
J.A. Dionne, L. Sweatlock, H.A. Atwater, and A. Polman, Phys. Rev. B **73**, 035407 (2006)

[5] *Plasmon-enhanced emission from optically-doped MOS light sources.*
A. C. Hryciw, Y. C. Jun, and M. L. Brongersma, Optics Express **17**, 1 (2008)

[6] *Excitation of surface plasmons at a SiO2-Ag interface by silicon quantum dots: Experiment and theory.*
J. Kalkman, H. Gersen, L. Kuipers, and A. Polman, Phys. Rev. B 73, 075317 (2006)